

Estimating the impact of a major hurricane on transport processes

Thomas Dobbelaere^{a,*}, Milan Curcic^b, Matthieu le Hénaff^{c,d}, Emmanuel Hanert^{a,e}

^a*Eath and Life Institute (ELI), UCLouvain, Louvain-la-Neuve, Belgium*

^b*Rosenstiel School of Marine and Atmospheric Sciences (RSMAS), University of Miami, Coral Gables, Florida, USA*

^c*Cooperative Institute for Marine and Atmospheric Studies (CIMAS), University of Miami, Miami, Florida, USA*

^d*Atlantic Oceanographic and Meteorological Laboratory (AOML), NOAA, Miami, Florida, USA*

^e*Institute of Mechanics, Materials and Civil Engineering (IMMC), UCLouvain, Louvain-la-Neuve, Belgium*

Abstract

In most hydrodynamic model studies, currents and waves are simulated separately. This is especially true for the simulation of passive drifters, whose trajectories are often computed based solely on currents. Although this simplification holds for most situations, as the force exerted by waves on currents can be neglected in fair weather conditions, it may lead to significant errors during storm conditions, when currents are strongly influenced by wind-generated waves. In this study, we investigate current-wave interactions in heavy-wind conditions by coupling the unstructured-mesh hydrodynamic model SLIM with the wave model SWAN. We apply the coupled model in the Florida Reef Tract during Hurricane Irma (Sep. 2017) and show that it successfully reproduces both the observed wave behavior

*Corresponding author

Email address: thomas.dobbelaere@uclouvain.be (Thomas Dobbelaere)

and storm surge during the hurricane. The modeled currents are then used to simulate the trajectories of passive drifters during the passage of the hurricane. Our results show that taking wave force into account induces variations of up 1 m/s in modelled currents on the continental shelf break as well as in the vicinity of reefs and islands. Wave-current interactions can therefore deflect the trajectories of drifting material by up to 10 km on the passage of the storm **Add something?**. These results strongly advocate for the inclusion of wave forces while studying transport processes (sediments, pollutants, larvae, etc.) in heavy-wind conditions.

Keywords:

¹ **1. Introduction**

² Wave-current interactions in coastal areas are of great importance for
³ coastal engineering as they play a key role in sediment transport, morpho-
⁴ logical evolution and pollutant mixing (Bever and MacWilliams, 2013; Li and
⁵ Johns, 1998). However, these interactions are highly nonlinear and can vary
⁶ significantly in space and time (Wu et al., 2011). Wave-induced currents are
⁷ generated by wave radiation gradients (Longuet-Higgins, 1970), affecting
⁸ water levels near shorelines and wave breaking points (Longuet-Higgins
⁹ and Stewart, 1964), while changes in water levels and currents, in turn,
¹⁰ affect the motion and evolution of the waves (Sikirić et al., 2013). Cou-
¹¹ pled wave-current models are therefore required to capture these complex
¹² interactions.

¹³ As coastal oceans are characterized by complex topology with islands,
¹⁴ inlets and estuaries, unstructured (usually two-dimensional) models are pre-
¹⁵ ferred as structured grid models show limitations in resolving topologically-
¹⁶ controlled nearshore processes (Wu et al., 2011; Chen et al., 2007). The
¹⁷ effect of wave-interactions becomes even more significant in the case of
¹⁸ hurricanes, that generate large wind-waves and disturb ocean conditions

19 (Liu et al., 2020) by causing coastal upwellings on continental shelves
20 (Smith, 1982) and inducing strong currents, waves and storm surges in
21 nearshore and coastal regions (Dietrich et al., 2010; Weisberg and Zheng,
22 2006).

23 South Florida and the Gulf of Mexico are particularly vulnerable to hur-
24 rricanes (Malmstadt et al., 2009) and modelling studies predict tropical
25 cyclones to increase both in frequency and intensity in this region (Mar-
26 sooli et al., 2019; Knutson et al., 2010). Being able to accurately model
27 wave-current interactions in this area becomes thus critical. *Expand...*

28 Individual-based modelling of particulates has been extensively used to
29 study the transport of drifting materials such as pollutants, sediments or
30 larvae (Garcia-Pineda et al., 2020; Liubartseva et al., 2018; Figueiredo
31 et al., 2013; Frys et al., 2020). Although some of these studies take the
32 impact of waves into account by adding a Stokes drift velocity, *i.e.* the net
33 drift of a floating particle in the direction of the wave propagation (Van
34 Den Bremer and Breivik, 2018), to the Eulerian currents, they usually
35 neglect the wave-induced currents. Such practice is reasonable in the
36 case of fair weather, when wave-induced forces exerted on currents are
37 relatively smaller, but might lead to significant inaccuracies during storm
38 conditions. To assess the importance of wave-current interactions during
39 a tropical cyclone, we investigated the transport of drifting particulates on
40 the Florida shelf during Hurricane Irma, one of the strongest and costliest
41 tropical cyclones on records in the Atlantic Basin (Chen et al., 2007), that
42 made landfall in Florida in September 2017.

43 In this study, we developed an unstructured coupled wave-current model of
44 South Florida to simulate the ocean circulation during hurricane Irma. Both
45 modelled currents and waves were validated against field measurements
46 and were then used to simulate the transport of drifting material in the
47 Florida Keys and the Florida inner shelf during the storm. Model outputs

48 were then compared with uncoupled simulation results in order to assess
49 the impact of wave-induced forces and Stokes drift on the modelled currents
50 and transports.

51 **2. Methods**

52 *2.1. Study area and observational data*

53 Large-scale ocean circulation around South Florida is dominated by the
54 Florida Current (FC), which originates from the Loop Currents (LC) where it
55 enters the Florida Straits from the Gulf of Mexico, and, downstream, forms
56 the Gulf Stream. The FC is a major western boundary current character-
57 ized by spatial variability and meandering, associated with the presence
58 of cyclonic eddies between the core of the current and the complex reef
59 topography of the Florida Reef Tract (FRT) (Lee et al., 1995; Kourafalou and
60 Kang, 2012). The northern half of these reefs are made of early Holocene
61 reef frameworks and indurated sand ridges while the southern part (the
62 Florida Keys) is composed of a chain of limestone islands, fossilized rem-
63 nants of ancient coral reefs and sand bars (Hoffmeister and Multer, 1968;
64 Shinn, 1988; Lidz and Shinn, 1991). The variability of the FC extends over
65 a large range of spatial and temporal scales, with periods of 30-70 days
66 in the Lower Keys (Lee et al., 1995) and shorter periods of 2-21 days in
67 the Upper Keys (Lee and Mayer, 1977), and exhibits significant seasonal
68 and interannual cycles (Johns and Schott, 1987; Lee and Williams, 1988;
69 Schott et al., 1988). Circulation on the West Florida Shelf (WFS) on the
70 other hand is forced by local winds and tidal fluctuations (Lee and Smith,
71 2002; Liu and Weisberg, 2012).

72 The state of the ocean around Florida is monitored by an extensive array of
73 tide gauges, current meters and buoys. In this study, we used sea surface
74 elevation measurements from the National Oceanic and Atmospheric Ad-
75 ministrations (NOAA) Tides and Currents dataset. These measurements

were taken at four locations: two in the Florida Keys (Key West and Vaca Key); one on the eastern coast of Florida (Key West); and one on the western coast (Naples). For the currents, we used ADCP measurements from the University of South Florida's College of Marine Science's (USF/CMS) Coastal Ocean Monitoring and Prediction System (COMPS) for the WFS (Weisberg et al., 2009). More specifically, we used measurements from moorings C10, C12 and C13, respectively located at the 25, 50, and 50 m isobaths of the WFS (Liu et al., 2020). Finally, for the waves, we used measurements from four buoys of the NOAA's National Data Buoy Center (NDBC). Two on Florida's Eastern shelf and two on the WFS. The locations of all measurement stations are shown on Fig. 1

2.2. Wind and atmospheric pressure during Hurricane Irma

Irma made landfall in Florida on 10 September 2017 as a category 3 storm, first at Cudjoe Key (Florida Keys) and later on Marco Island, south to Naples (see hurricane track in Fig. 1). It then weakened to a category 2 storm as it moved further inland (Pinelli et al., 2018). The storm caused damages to up to 75% of the buildings at his landfall point in the Florida Keys, making it one of the strongest and costliest hurricanes on record in the Atlantic basin (Xian et al., 2018; Zhang et al., 2019). The strongest reported wind speed was 50 m/s on Marco Island while the highest recorded storm surge was 2.3 m, although larger wind speed likely occurred in the Florida Keys (Pinelli et al., 2018). In order to reproduce the wind profile of Irma in our model, we used high-resolution H*Wind wind fields (Powell et al., 1998). As these data represent 1-min averaged wind speeds, we multiplied them by a factor 0.93 to obtain 10-min averaged wind speeds (Harper et al., 2010), which are more consistent with the time step of our model. Furthermore, H*Wind wind profiles did not cover the whole model extent during the hurricane and were thus blended within coarser wind field extracted from ECMWF ERA-5 datasets. Pressure fields of Irma were also constructed using ERA-5 data.

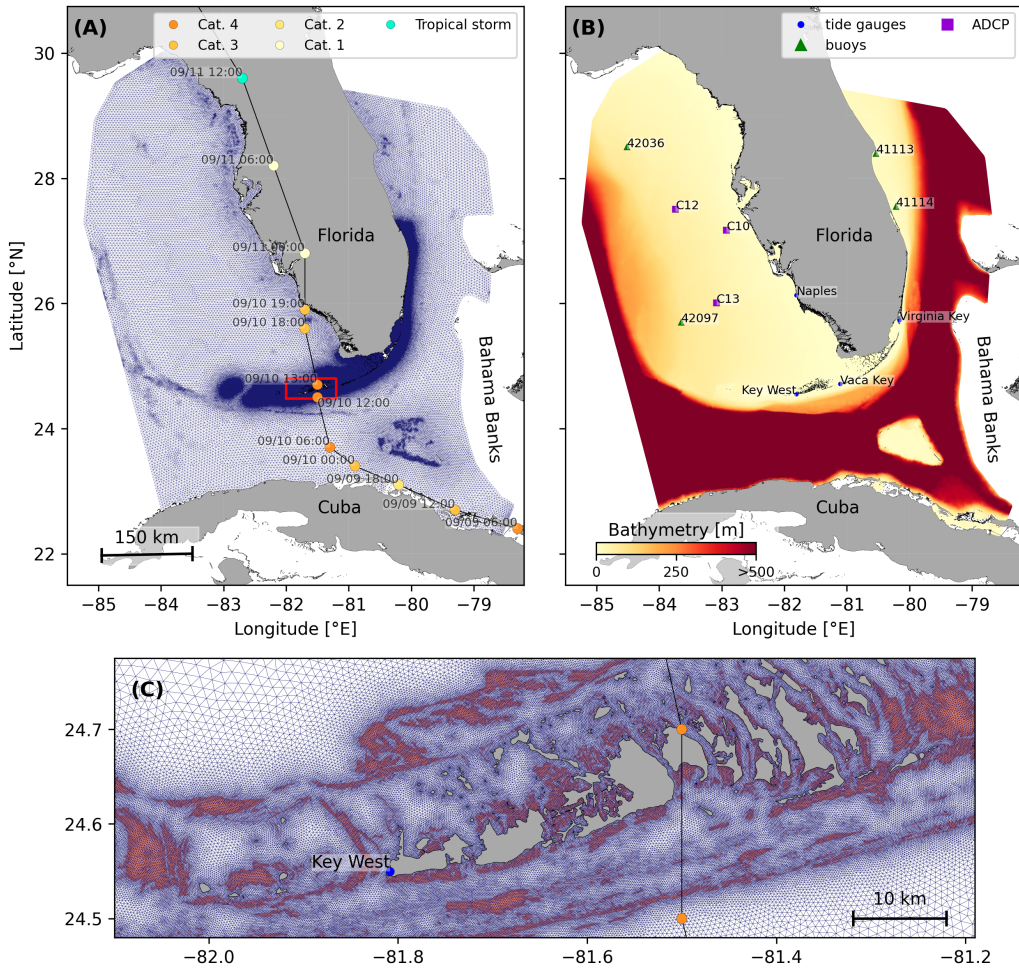


Fig. 1: **A:** Mesh of the computational domain with the trajectory of Irma, category of the hurricane is given by the Saffir-Simpson color scale. **B:** Bathymetry of the domain with the location of stations used for the validation of the model outputs. **C:** Close up view of the Lower Keys area, where the mesh resolution reaches 100m near reefs (shown in coral) and islands (highlighted in dark grey)

105 However, the coarse resolution of the dataset smooth out the depression at
 106 the center of the hurricane, leading to an underestimation of the pressure
 107 gradient in our model. To better capture the central depression of Irma, we
 108 built a hybrid pressure field using the position and the minimal pressure of
 109 the core of the hurricane based on its track as recorded in the HURDAT
 110 2 database (Landsea and Franklin, 2013). Based on this information, the
 111 hybrid pressure field was constructed by combining an idealized Holland
 112 pressure profile (Lin and Chavas, 2012) within the radius of maximum
 113 wind speed of Irma (Knaff et al., 2018) with ERA-5 pressure field. The
 114 transition between from the Holland profile to ERA-5 data outside the radius
 115 of maximum wind speed data was performed using a smooth step function.

116 *2.3. Hydrodynamic model*

117 Ocean currents generated during hurricane Irma around South Florida were
 118 modelled using the 2D barotropic version of the unstructured-mesh coastal
 119 ocean model SLIM¹. The model mesh covers an area similar to the model
 120 extent of Dobbelaere et al. (2020b), that includes the FRT but also the
 121 Florida Strait and part of the Gulf of Mexico (Figure 1). However, this area
 122 has been slightly extended northeastward and westward in order to include
 123 the NOAA-NDBC buoys. Furthermore, in order to withstand potential cell
 124 drying during the hurricane, we solved the conservative shallow water
 125 equations with wetting-drying:

$$\begin{aligned}
 \frac{\partial H}{\partial t} + \nabla \cdot (\mathbf{U}) &= 0 , \\
 \frac{\partial \mathbf{U}}{\partial t} + \nabla \cdot \left(\frac{\mathbf{U}\mathbf{U}}{H} \right) &= - f\mathbf{e}_z \times \mathbf{U} + \alpha g H \nabla(H - h) - \frac{1}{\rho} \nabla p_{\text{atm}} + \frac{1}{\rho} \boldsymbol{\tau}_s \quad (1) \\
 &\quad + \nabla \cdot (\nu \nabla \mathbf{U}) - \frac{C_b}{H^2} |\mathbf{U}| \mathbf{U} + \gamma (\mathbf{U}_* - \mathbf{U}) ,
 \end{aligned}$$

¹<https://www.slim-ocean.be>

126 where H is the water column height and \mathbf{U} is the depth-averaged transport;
 127 f is the Coriolis coefficient; g is the gravitational acceleration; h is the
 128 bathymetry; α is a coefficient stating whether the mesh element is wet
 129 ($\alpha = 1$) or dry ($\alpha = 0$); ν is the viscosity; C_b is the bulk bottom drag
 130 coefficient; ∇p_{atm} is the atmospheric pressure gradient; τ_s is the surface
 131 stress due to wind; and γ is a relaxation coefficient towards a reference
 132 transport \mathbf{U}_* . As in Frys et al. (2020) and Dobbelaere et al. (2020b), SLIM
 133 currents were gradually relaxed towards HYCOM (Chassignet et al., 2007)
 134 in regions where the water depth exceeds 50m.

135 At very high wind speeds, the white cap is blown off the crest of the waves,
 136 which generates a layer of droplets that acts as a slip layer for the winds
 137 at the ocean-atmosphere interface (Holthuijsen et al., 2012). This causes
 138 a saturation of the wind drag coefficient for strong winds (Donelan et al.,
 139 2004; Powell et al., 2003). To account for the impact of this saturation
 140 on the surface wind stress in our model, we implemented the wind drag
 141 parameterization of Moon et al. (2007). In this parameterization, the drag
 142 coefficient C_d depends on the wind speed at 10-m height U_{10} according to:

$$C_d = \kappa^2 \log \left(\frac{10}{z_0} \right)^{-2} \quad (2)$$

143 where κ is the von Karman constant. The roughness length z_0 in Eq. (2) is
 144 expressed as:

$$z_0 = \begin{cases} \frac{0.0185}{g} U_*^2 & \text{if } U_{10} \leq 12.5 \text{ m/s ,} \\ [0.085(-0.56U_*^2 + 20.255U_* + 2.458) - 0.58] \times 10^{-3} & \text{if } U_{10} > 12.5 \text{ m/s ,} \end{cases} \quad (3)$$

145 with U_* the friction velocity. The relation between U_{10} and U_* is given by:

$$U_{10} = -0.56U_*^2 + 20.255U_* + 2.458 . \quad (4)$$

146 The mesh resolution depends on the distance to coastlines and reefs
 147 following the approach of Dobbelaere et al. (2020b). The mesh is then
 148 further refined according to bathymetry value and gradient, as suggested in
 149 the SWAN user-guide². Such an approach improves the model efficiency
 150 as the mesh resolution is only increased where required by the currents and
 151 waves dynamics. The mesh was generated with the seamsh³ Python library,
 152 which is based on the the open-source mesh generator GMSH (Geuzaine
 153 and Remacle, 2009). It is composed of approximately 7.7×10^5 elements.
 154 The coarsest elements, far away from the FRT, has a characteristic length
 155 of about 5 km whereas the finest elements have a characteristic length of
 156 about 100 m near coastlines and reefs (Fig 1).

157 *2.4. Wave model*

158 Waves were modelled using the parallel unstructured-mesh version of the
 159 Simulating WAves Nearshore (SWAN) model (Booij et al., 1999), one of
 160 the most commonly used wave models in coastal areas and inland waters.
 161 This model solves the action balance equation (Mei, 1989):

$$\frac{\partial N}{\partial t} + \nabla_{\mathbf{x}} \cdot [(\mathbf{c}_g + \mathbf{u})N] + \frac{\partial}{\partial \theta}[c_\theta N] + \frac{\partial}{\partial \sigma}[c_\sigma N] = \frac{S_{in} + S_{ds} + S_{nl}}{\sigma}, \quad (5)$$

162 where $N = E/\sigma$ is the wave action density; θ is the wave propagation
 163 direction; σ is the wave relative frequency; \mathbf{c}_g is the wave group velocity, $\mathbf{u} =$
 164 \mathbf{U}/H is SLIM depth-averaged current velocity; c_θ and c_σ are the propagation
 165 velocities in spectral space due to refraction and shifting in frequency
 166 due to variations in depth and currents; and S_{in} , S_{ds} , and S_{nl} respectively
 167 represent wave growth by wind, wave decay and nonlinear transfers of wave
 168 energy through interactions between triplets and quadruplets. Spectra were
 169 discretized with 48 direction bins and 50 frequency bins logarithmically

²<http://swanmodel.sourceforge.net/unswan/unswan.htm>

³<https://pypi.org/project/seamsh/>

distributed from 0.3 to 2 Hz. Exponential wind growth was parameterized using the formulation of Janssen (1991), while dissipations by whitecapping and bottom dissipations followed the formulations of Komen et al. (1984) and Madsen et al. (1989) respectively. Coefficients for exponential wind growth and whitecapping parameterizations were based on the results of Siadatmousavi et al. (2011), and significantly differ from SWAN's default settings. By default, SWAN implements the wind input formulation of Komen et al. (1984) and the steepness-dependent coefficient governing dissipation by whitecapping is a linear function of the wave number. In this study, this steepness-dependent coefficient is a quadratic function of the wave number, as it showed better predictions of the significant wave height in the study of Siadatmousavi et al. (2011). The choice of these formulations was motivated by the appearance of numerical instabilities in the region of the Gulf Stream when using SWAN's default parameter values. Finally, wave boundary conditions were derived from WAVEWATCH III (Tolman et al., 2009) spectral outputs at buoy locations.

Surface waves induce a net drift in the direction of the wave propagation, known as the Stokes drift (Van Den Bremer and Breivik, 2018; Stokes, 1880). This net drift has a significant impact on sediment transport in near shore regions (Hoefel and Elgar, 2003), on the formation of Langmuir cells (Langmuir, 1938; Craik and Leibovich, 1976) as well as on the transport of heat, salt or pollutants such as oil or micro-plastic in the upper ocean layer (McWilliams and Sullivan, 2000; Röhrs et al., 2012; Drivedal et al., 2014). To correctly model the Stokes drift profile in mixed wind-driven sea and swell conditions, the full two-dimensional wave spectrum must be represented by a spectral wave model within a wave-current coupling (Van Den Bremer and Breivik, 2018). In this study, depth-averaged Stokes drift was therefore computed by SWAN using the following formula:

$$\mathbf{u}_s = \int_0^{2\pi} \int_0^{+\infty} \frac{\sigma^3}{h \tanh(2kh)} E(\sigma, \theta) (\cos \theta, \sin \theta) d\sigma d\theta , \quad (6)$$

198 where k is the norm of the wave vector; h is the water depth; and $E(\sigma, \theta)$ is
199 the wave energy density.

200 *2.5. Coupled model*

201 SLIM and SWAN are coupled so that they run on the same computational
202 core and the same unstructured mesh. SLIM is run first and passes com-
203 puted wind velocities (\mathbf{U}_{10}), water levels ($\eta = H - h$) and depth-averaged
204 currents ($\mathbf{u} = \mathbf{U}/H$) to SWAN, as well as a roughness length (z_0) for the
205 bottom dissipation formulation of Madsen et al. (1989). This roughness
206 length is computed from SLIM's bulk drag coefficient C_b following the ap-
207 proach of Dietrich et al. (2011) so that both models have consistent bottom
208 dissipation parameterizations. SWAN then utilizes these quantities to com-
209 pute the wave radiation stress gradient, that is then passed to SLIM as
210 the wave-induced stress on currents τ_{wave} (Fig. 2). SLIM then uses this
211 quantity to update the the value of the surface stress τ_s in Eq. (1), that now
212 becomes the sum of wind and wave-induced stresses $\tau_s = \tau_{\text{wind}} + \tau_{\text{wave}}$.

213 SLIM's governing equations are integrated using an implicit time integration
214 scheme while SWAN is unconditionally stable (*say that you use the steady*
215 *version, explain the difference with the unsteady version*) (Dietrich et al.,
216 2010), allowing both models to be run with relatively large time steps. In
217 this study, both models were therefore run sequentially using a time step
218 of 600s, so that each computational core was alternating running either
219 SLIM or SWAN. As in the coupling between SWAN and ADCIRC (Dietrich
220 et al., 2010), both models utilize the same local sub-mesh, allowing for a
221 one-to-one correspondence between the geographic locations of the mesh
222 vertices. No interpolation is therefore needed when passing the discretised
223 variables from one model to the other, which allows an efficient inter-model
224 communication. However, as SLIM applies discontinuous Galerkin finite
225 element methods, an additional conversion step to a continuous framework
226 was required to transmit SLIM nodal quantities to SWAN.

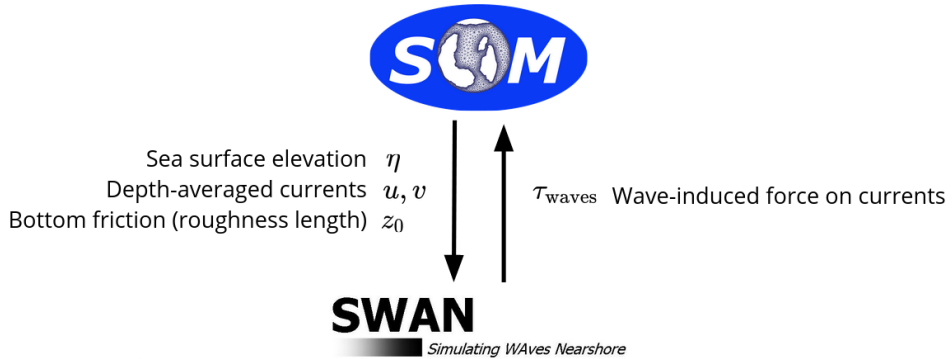


Fig. 2: Schematic illustration of the coupled SLIM+SWAN model.

227 3. Results

228 We first validated the reconstructed atmospheric fields of hurricane Irma as
 229 well the modelled currents and waves of our coupled model against fields
 230 measurements. We then use the validated model to simulate the transport
 231 of passive drifters in the Lower Keys during the passage of the hurricane.
 232 These drifters were advected by two sets of currents: (i) the currents
 233 from an uncoupled SLIM simulation of Irma (SLIM) and (ii) the currents
 234 modelled by the coupled SLIM+SWAN model (SLIM+SWAN). Furthermore,
 235 the depth-averaged Stokes drift was computed using our coupled model
 236 (Stokes_C) and an uncoupled SWAN simulation of the hurricane (Stokes_U).
 237 We then simulated the trajectories of passive drifters during the passage
 238 of the Irma in the Lower Keys using different combinations of these fields.
 239 These trajectories were finally compared to evaluate the impact of the
 240 wave-current interactions and the Stokes drift on the transport processes
 241 during a major hurricane.

242 3.1. Model validation

243 H*Wind winds and hybrid pressure field agree well with station measure-
 244 ments at Vaca Key station (Fig. 3). The hybrid pressure field shows better

Validation of atmospheric forcings at Vaca Key station

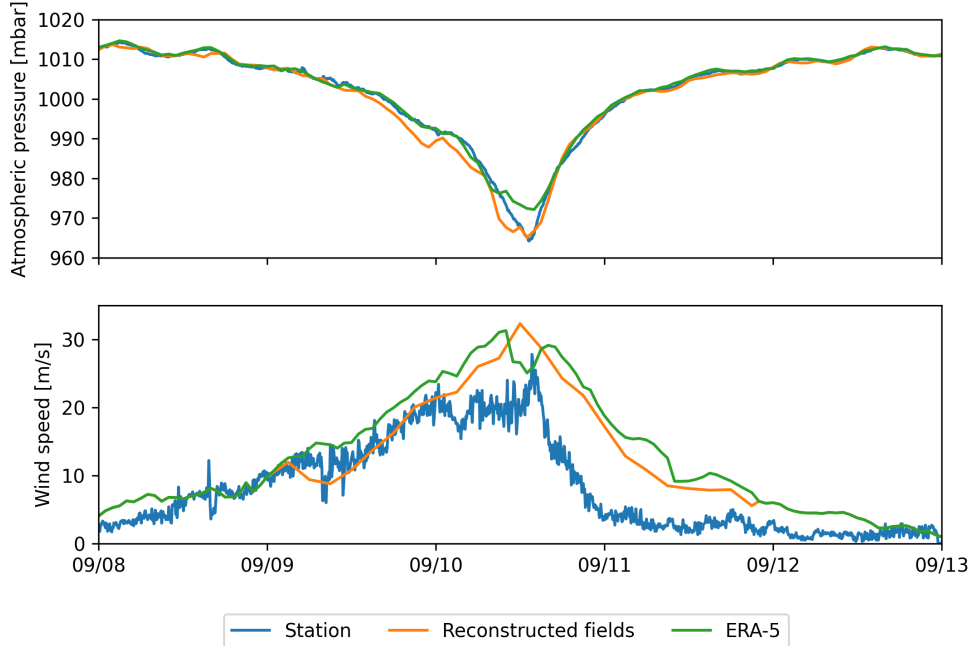


Fig. 3: Comparison of reconstructed wind atmospheric pressure with field measurements and coarser ECMWF ERA-5 profiles at Vaca Key station. The generated hybrid atmospheric forcings better capture the observed storm depression while H*wind winds better match the measured peak in wind speed.

agreement with observations than ERA-5 pressure as it successfully reproduces the storm depression. ERA-5 fields, on the other hand, fail to resolve the low pressure at the core of the hurricane due to their coarser grid, leading to an overestimation of 8 mbar of the storm depression. Both H*Wind and ERA-5 agree well with observed wind speeds although both data sets tend to slightly overestimate the width and intensity of the wind peak. However, H*wind profiles show a better match with the timing of the observed peak, as ERA-5 winds tend to anticipate it. H*wind also exhibits a slightly narrower peak in wind speed, which better agrees with observations.

Hydrodynamic outputs of the coupled wave-current agree well with tide

gauge (Fig. 4) and ADCP measurements (Fig. 5). The timing and amplitude of the storm surges are well reproduced by the coupled model, the largest model error being an overestimation of 18 cm of the elevation peak at Virginia Key. The fit is especially good at Naples, where both the positive and negative surges are captured by the coupled model with an error of less than 5 cm. This result is of interest as negative surges, although less studied, affect water exchanges between the estuaries and the coastal ocean and disturb the benthic ecosystems (Liu et al., 2020). Modelled 2D currents were validated against depth-averaged ADCP measurements at mooring station C10, C12 and C13 (Fig. 5). As in Liu et al. (2020), we performed the vector correlation analysis of Kundu (1976) to compare modelled and observed current velocity vectors. Correlation coefficients (ρ) between simulated and observed depth-averaged currents were 0.84, 0.74 and 0.73 at the C10, C12 and C13 locations, respectively. Average veering angles were computed as well and were below 12° , as in (Liu et al., 2020). However, in our case, no clear tendency regarding modelled current behavior compared to observations was observed. As expected from a depth-averaged model, the best fit with observations is obtained at the shallowest mooring C10, located on the 25m isobath, with an average veering angle of 6° .

The simulated significant wave height agrees well with observations on the WFS, where errors on the peak value do not exceed 5% (Fig. fig:waves). On the East Florida Shelf, errors are slightly larger and reach 20%. Although the model outputs agree well with observations, a lag in significant wave height is observed for all 4 buoys. Moreover, the peak in significant wave height tends to be underestimated at buoys 41113 and 41114, located on the East Florida Shelf. Other wave parameters were better reproduced by the model on the WFS as well (see buoy 42036 in Fig. 6). This good fit on the WFS is not surprising as the parameters used for wind energy input and whitecapping dissipation were based on the calibration performed

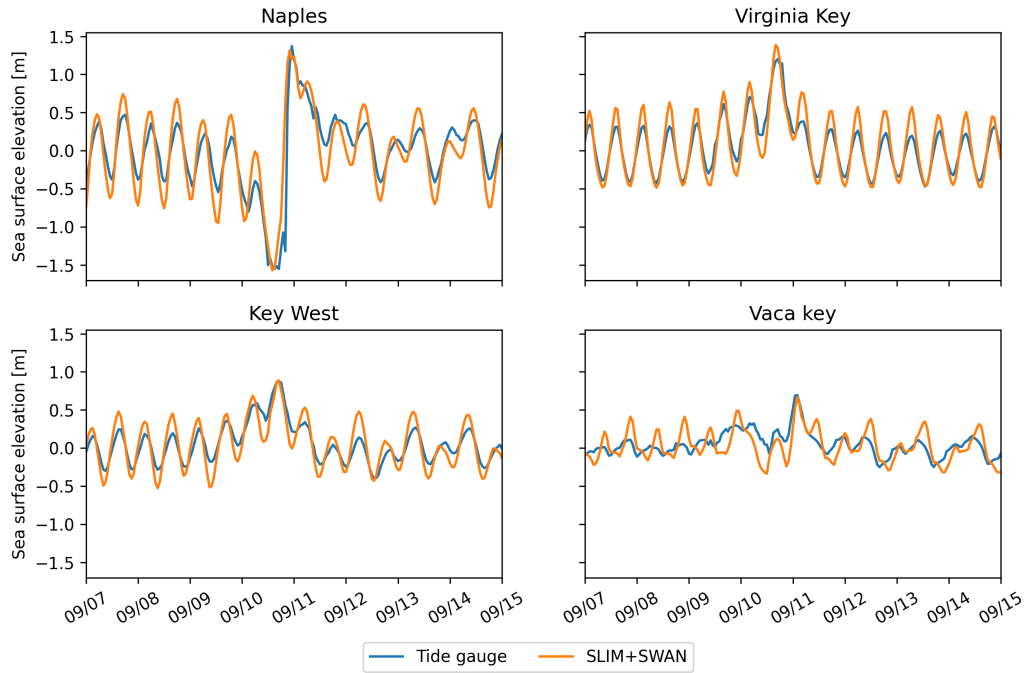


Fig. 4: Comparison of modelled sea surface elevation with all 4 tide gauge measurements (see Fig. 1B for their location). Timing and amplitudes of the storm surges are well reproduced by the model

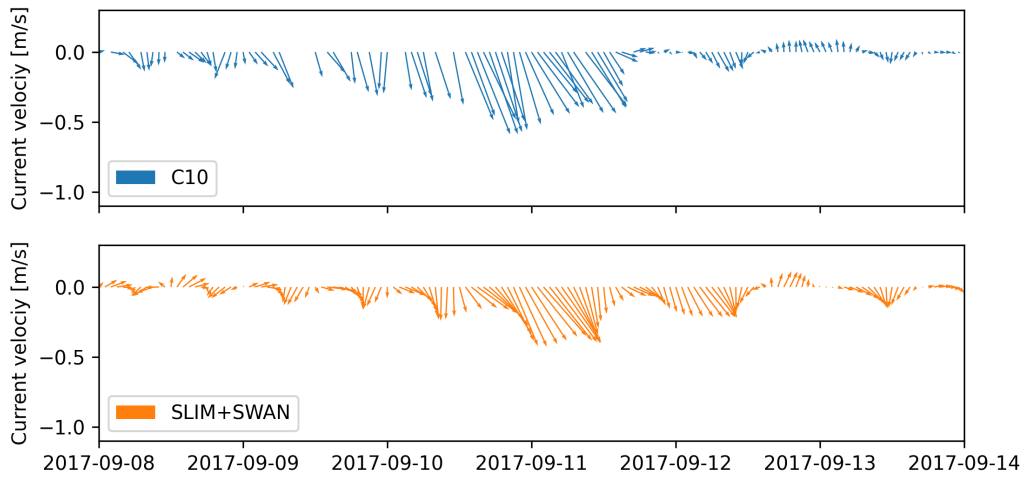


Fig. 5: Comparison of modelled current velocity with observed velocity at mooring C10 (see Fig. 1B for its location). Modelled current velocities agree well with observations, with a correlation coefficient of 0.83 and an average veering angle of 6° .

286 by Siadatmousavi et al. (2011) on the Northern Gulf of Mexico. Wind-
287 induced wave growth might therefore be underestimated on the eastern
288 shelf. Consequently, incident wave do not receive enough energy to grow
289 after breaking on the bank boundary, leading to an underestimation of the
290 significant wave height at the location of the buoys. Nonetheless, as this
291 study focused on the wave produced by Irma, that made landfall on the
292 western coasts of Florida, the use of parameterizations calibrated for the
293 Gulf of Mexico seems reasonable.

294 *3.2. Impact of waves on currents and transport*

295 We evaluated the impact of wave-current interactions on modelled currents
296 during the passage of Irma in the Lower Keys, between Sept. 7 and
297 13, 2017. First, we computed the maximum difference between currents
298 modelled by SLIM and SLIM+SWAN during this period (Fig. 7A). The
299 largest differences in current speed were observed over the reefs, on the
300 shelf break and around islands. They can locally reach 1 m/s, with the
301 coupled model SLIM+SWAN yielding the largest amplitudes. The regions
302 where the differences are the largest experience the largest wave-induced
303 stress τ_{wave} (7B), as wave breaking and wave slowing down over rough
304 seabed induce variations of the wave radiation stress (Longuet-Higgins and
305 Stewart, 1964). Wave-induced differences in current speed were amplified
306 by the action of the wind stress τ_{wind} (Fig. 7C). Wind speeds were larger
307 in the front right quadrant of the hurricane (Zedler et al., 2009), yielding
308 larger differences on the right-hand side of the storm trajectory. This is
309 especially clear in the area between the Florida Keys and the Everglades,
310 where relatively small values of τ_{wave} nonetheless produce current speed
311 differences of up to 0.5 m/s because of the wind stress.

312 To quantify the impact of these differences in the velocity fields, we com-
313 pared the trajectories of passive particles advected by the uncoupled SLIM
314 and coupled SLIM+SWAN currents during the passage of Irma in the Lower

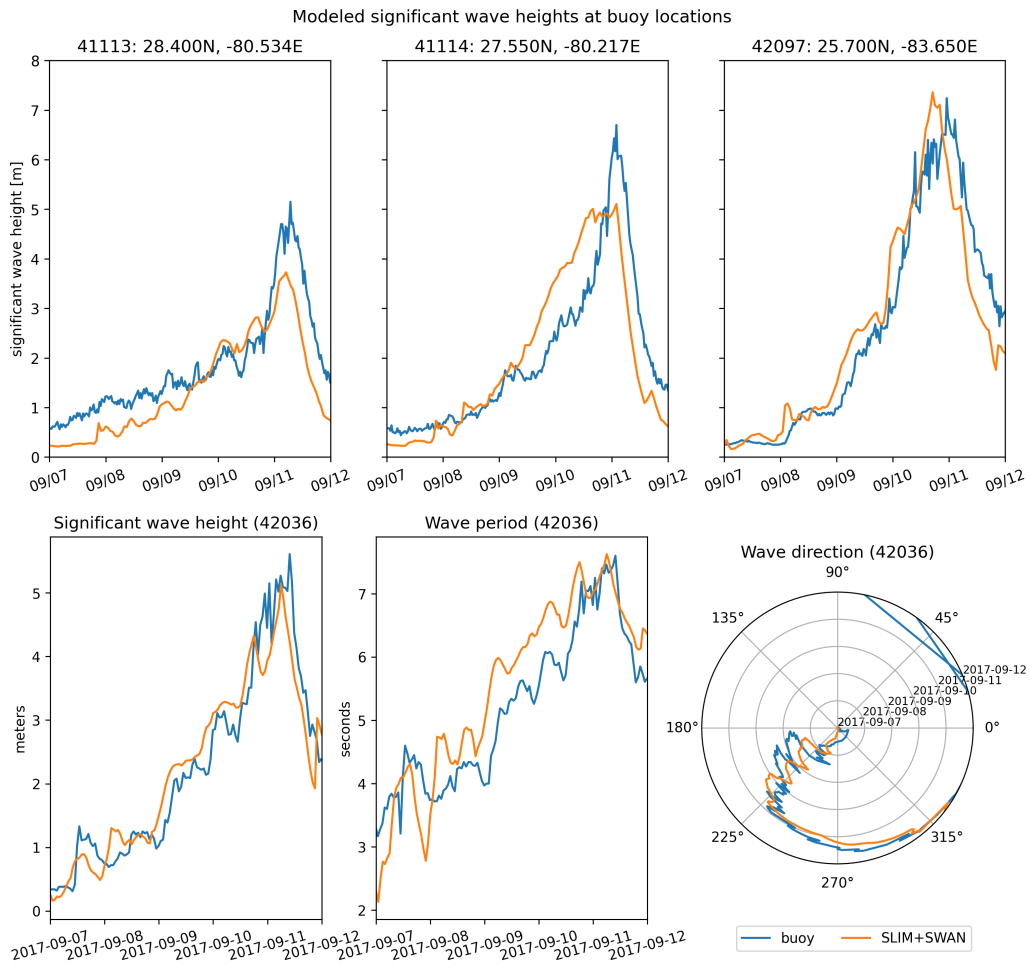


Fig. 6: Comparison of modelled wave parameters with observation at the 4 buoys location (locations shown in Fig. 1B). Modelled significant wave height agrees well with field measurement. As model parameters were calibrated for the Northern Gulf of Mexico, observations are better reproduced at buoys located on the WFS, as illustrated for buoy 42036

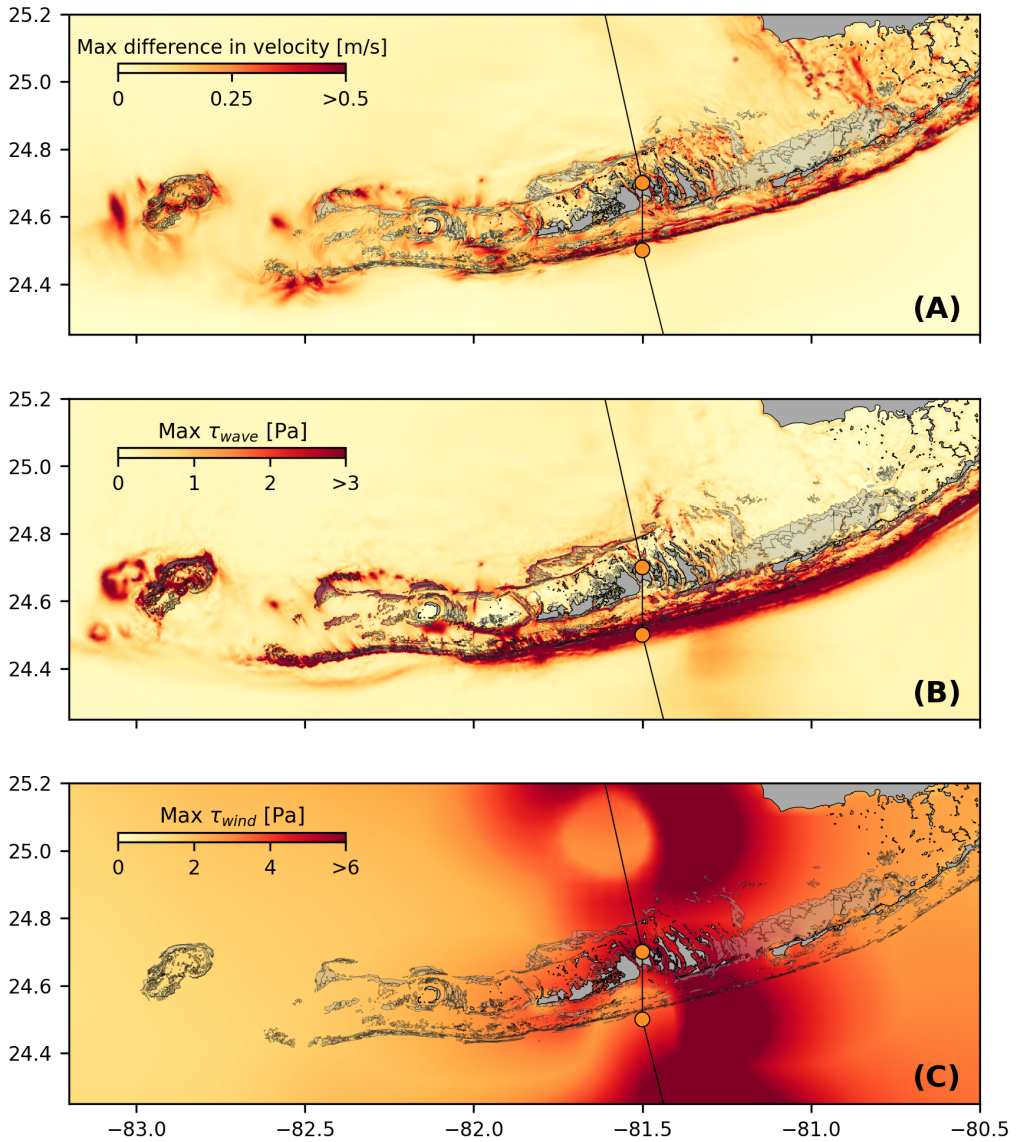


Fig. 7: Maximum difference between SLIM and SLIM+SWAN currents (A) during the passage of Irma in the Lower Florida Keys, along with the maximum wave radiation stress gradient τ_{wave} (B) and wind stress τ_{wind} (C) generated by the hurricane. Wave-induced stress yields difference larger than 0.5 m/s in current velocities. These wave-induced differences in currents were amplified by the action of the asymmetric wind profile of Irma, with larger differences occurring on the right of the storm trajectory

315 Keys (Fig. 8). Particles were released on the inner and outer shelves at
316 the points highlighted in red and blue circles in Fig. 8A on 7 September
317 and then tracked until 15 September. These areas were constructed using
318 backtracking methods (Dobbelaeere et al., 2020a) to ensure that the release
319 particles would intersect the path of Irma during its passage in the Florida
320 Keys. We first defined two 25km^2 circular regions on the trajectory of the
321 hurricane (see red and blue circles in Fig. 8A). Particles within these two
322 regions were then tracked backward in time using uncoupled SLIM currents
323 from the exact time of the passage of the hurricane until the 7th of Septem-
324 ber. Their positions at the end of the backward simulation (see red and blue
325 particle clouds in Fig. 8) corresponds to the initial condition of the forward
326 transport simulations described below.

327 We compared the trajectories of particles originating from these regions and
328 advected forward in time by different sets of currents: (i) uncoupled SLIM
329 currents alone; (ii) coupled SLIM+SWAN currents; (iii) SLIM currents with
330 the addition of the depth-averaged Stokes drift computed by the coupled
331 wave model (Stokes_C); (iv) SLIM+SWAN currents with Stokes_C; and
332 (v) SLIM currents with the depth-averaged Stokes drift computed by the
333 uncoupled wave model (Stokes_U). Particles trajectories are compared by
334 computing the distances between the centers of mass of the particle clouds
335 through time. Here are our main observations (*this needs to be improved,*
336 *feedback is welcome!*) :

- 337 • The impact of wave-current interactions is most important during the
338 passage of the hurricane but negligible during the rest of the simulated
339 period. This is clear when comparing the clouds of particles advected
340 by SLIM and SLIM+SWAN on the outer shelf. The distance between
341 the centers of mass reaches 5 km during the passage of Irma but
342 tends to zero during the rest of the simulated period.
- 343 • The impact of the Stokes drift is larger than the impact of the wave-

344 current interactions on the inner shelf. The difference between the cen-
345 ters of mass does not exceed about 1 km for SLIM vs SLIM+SWAN but
346 reaches about 5 km for SLIM vs SLIM+Stokes_C and SLIM+SWAN+Stokes_C.
347 On the outer shelf, the currents are more intense and the impact the
348 wave-current coupling during the passage of the hurricane is suffi-
349 cient to generate a difference between the two clouds of particles
350 that keeps on increasing after the passage of the hurricane. The
351 impact of the Stokes drift remains however larger than the impact
352 of the wave-current coupling. This difference between the inner and
353 outer shelf can be explained by the sheltering of the inner shelf due
354 to reefs and islands as well as wave breaking on the shelf break. The
355 inner shelf hence experiences weaker waves and weaker currents,
356 and hence also weaker and more localised transport.

- 357 • On the inner shelf, the distance between the centers of mass of the
358 particle clouds stabilizes after the passage of the hurricane while this
359 distance keeps increasing during a couple of days after the passage
360 of the hurricane on the outer shelf under the action of the Stokes drift.
361 This shows the strong impact of wave-induced transport in the open
362 ocean.
- 363 • Impact of Stokes drift and wave-current interactions weaker on the
364 inner shelf. Max. distance of about 5 km between the centers of mass
365 of the clouds of particles compared to 30km on the outer shelves
- 366 • The fact that SLIM+Stokes_C vs. SLIM+Stokes_U keeps increasing
367 on the outer shelf after the passage of the hurricane shows the impact
368 of the strong current velocities of the FC on the modelled Stokes drift
- 369 • Nonetheless, the differences between the coupled and uncoupled
370 Stokes drifts remains relatively small with a maximum value of 2 km
371 between the centers of mass of the simulated particle clouds. Further-
372 more, as SLIM vs SLIM+SWAN+Stokes and SLIM vs. SLIM+Stokes_C

373 show similar values on the inner shelf, this suggests that the combina-
374 tion of currents and Stokes drifts produces sufficiently accurate results
375 on sheltered shallow areas such as the WFS. However, neglecting
376 the wave-current interactions leads to differences of up to 5 km in
377 modelled particle trajectories on the outer shelf.

378 4. Discussion

379 Impact of waves on coral connectivity

380 Ability of wave model to correctly capture gradient in significant wave height
381 due to current-waves interactions under tropical cyclones depends on:

- 382 • Broad perspective \Rightarrow not limited to FL
- 383 • Mention search and rescue
- 384 • However, ignoring waves in storm conditions could result in significant
385 inaccuracies in modelled trajectories, as illustrated in the case of
386 release region 2 in Fig. 8
- 387 • Spatial (10km \rightarrow 5km) and spectral (36 dir. \rightarrow 48 dir.) resolution
388 (Hegermiller et al., 2019)
- 389 • Directional spreading of incident waves (Villas Bôas et al., 2020)

390 5. Conclusion

391 Acknowledgments

392 Computational resources were provided by the Consortium des Équipements
393 de Calcul Intensif (CÉCI), funded by the F.R.S.-FNRS under Grant No.
394 2.5020.11. Thomas Dobbelaere is a PhD student supported by the Fund
395 for Research training in Industry and Agriculture (FRIA/FNRS).

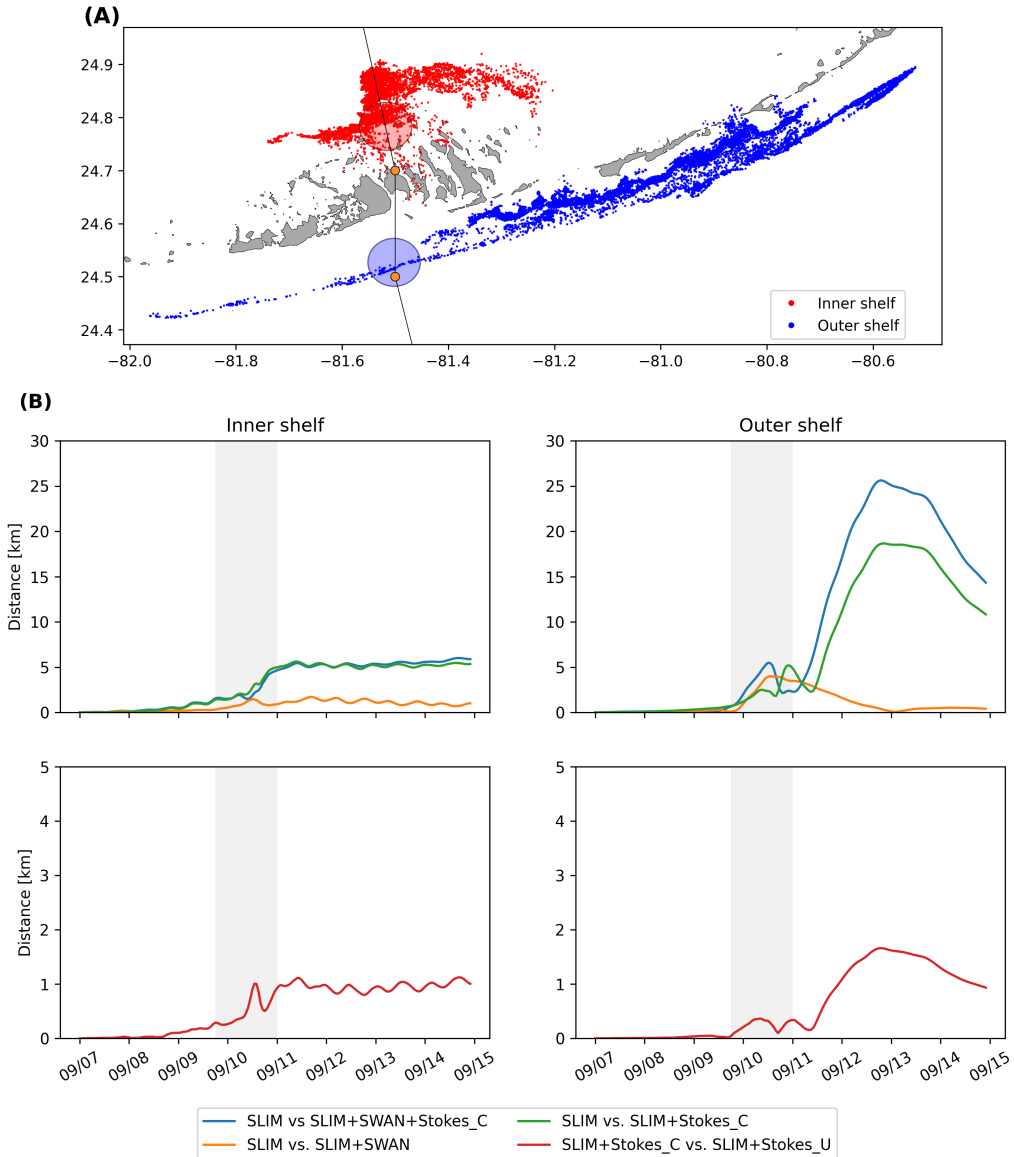


Fig. 8: **A:** Release regions of the passive particles on the inner and outer shelves (red and blue clouds) obtained by backtracking particles released in the red and blue circular areas during the passage of Irma. **B:** Difference between the centers of mass of the particle clouds released from the regions highlighted in **A** and advected by different combinations of coupled and uncoupled velocity fields.

396 **References**

- 397 Bever, A.J., MacWilliams, M.L., 2013. Simulating sediment transport pro-
398 cesses in San Pablo Bay using coupled hydrodynamic, wave, and sedi-
399 ment transport models. *Marine Geology* 345, 235–253.
- 400 Booij, N., Ris, R.C., Holthuijsen, L.H., 1999. A third-generation wave model
401 for coastal regions: 1. Model description and validation. *Journal of
402 geophysical research: Oceans* 104, 7649–7666.
- 403 Chassignet, E.P., Hurlburt, H.E., Smedstad, O.M., Halliwell, G.R., Hogan,
404 P.J., Wallcraft, A.J., Baraille, R., Bleck, R., 2007. The HYCOM (hybrid
405 coordinate ocean model) data assimilative system. *Journal of Marine
406 Systems* 65, 60–83.
- 407 Chen, C., Huang, H., Beardsley, R.C., Liu, H., Xu, Q., Cowles, G., 2007.
408 A finite volume numerical approach for coastal ocean circulation stud-
409 ies: Comparisons with finite difference models. *Journal of Geophysical
410 Research: Oceans* 112.
- 411 Craik, A.D., Leibovich, S., 1976. A rational model for Langmuir circulations.
412 *Journal of Fluid Mechanics* 73, 401–426.
- 413 Dietrich, J., Bunya, S., Westerink, J., Ebersole, B., Smith, J., Atkinson, J.,
414 Jensen, R., Resio, D., Luettich, R., Dawson, C., et al., 2010. A high-
415 resolution coupled riverine flow, tide, wind, wind wave, and storm surge
416 model for southern Louisiana and Mississippi. part ii: Synoptic description
417 and analysis of hurricanes Katrina and Rita. *Monthly Weather Review* 138,
418 378–404.
- 419 Dietrich, J., Westerink, J., Kennedy, A., Smith, J., Jensen, R., Zijlema,
420 M., Holthuijsen, L., Dawson, C., Luettich, R., Powell, M., et al., 2011.
421 Hurricane Gustav (2008) waves and storm surge: Hindcast, synoptic

- 422 analysis, and validation in southern Louisiana. *Monthly Weather Review*
423 139, 2488–2522.
- 424 Dobbelaere, T., Muller, E., Gramer, L., Holstein, D., Hanert, E., 2020a.
425 Report on the potential origin of the SCTLD in the Florida Reef Tract.
426 Available online at: [https://floridadep.gov/rcp/coral/documents/
427 report-potential-origin-sctld-florida-reef-tract](https://floridadep.gov/rcp/coral/documents/report-potential-origin-sctld-florida-reef-tract).
- 428 Dobbelaere, T., Muller, E.M., Gramer, L.J., Holstein, D.M., Hanert, E., 2020b.
429 Coupled epidemio-hydrodynamic modeling to understand the spread of
430 a deadly coral disease in Florida. *Frontiers in Marine Science* 7, 1016.
- 431 Donelan, M., Haus, B., Reul, N., Plant, W., Stiassnie, M., Graber, H., Brown,
432 O., Saltzman, E., 2004. On the limiting aerodynamic roughness of the
433 ocean in very strong winds. *Geophysical Research Letters* 31.
- 434 Drivdal, M., Broström, G., Christensen, K., 2014. Wave-induced mixing
435 and transport of buoyant particles: application to the statfjord a oil spill.
436 *Ocean Science* 10, 977–991.
- 437 Figueiredo, J., Baird, A.H., Connolly, S.R., 2013. Synthesizing larval com-
438 petence dynamics and reef-scale retention reveals a high potential for
439 self-recruitment in corals. *Ecology* 94, 650–659.
- 440 Frys, C., Saint-Amand, A., Le Hénaff, M., Figueiredo, J., Kuba, A., Walker,
441 B., Lambrechts, J., Vallaeys, V., Vincent, D., Hanert, E., 2020. Fine-scale
442 coral connectivity pathways in the Florida Reef Tract: implications for
443 conservation and restoration. *Frontiers in Marine Science* 7, 312.
- 444 Garcia-Pineda, O., Androulidakis, Y., Le Hénaff, M., Kourafalou, V., Hole,
445 L.R., Kang, H., Staples, G., Ramirez, E., DiPinto, L., 2020. Measuring
446 oil residence time with GPS-drifters, satellites, and Unmanned Aerial
447 Systems (UAS). *Marine pollution bulletin* 150, 110644.

- 448 Geuzaine, C., Remacle, J.F., 2009. Gmsh: A 3-d finite element mesh
449 generator with built-in pre-and post-processing facilities. International
450 journal for numerical methods in engineering 79, 1309–1331.
- 451 Harper, B., Kepert, J., Ginger, J., 2010. Guidelines for converting between
452 various wind averaging periods in tropical cyclone conditions. Citeseer.
- 453 Hegermiller, C.A., Warner, J.C., Olabarrieta, M., Sherwood, C.R., 2019.
454 Wave-current interaction between Hurricane Matthew wave fields and
455 the Gulf Stream. Journal of Physical Oceanography 49, 2883–2900.
- 456 Hoefel, F., Elgar, S., 2003. Wave-induced sediment transport and sandbar
457 migration. Science 299, 1885–1887.
- 458 Hoffmeister, J., Multer, H., 1968. Geology and origin of the Florida Keys.
459 Geological Society of America Bulletin 79, 1487–1502.
- 460 Holthuijsen, L.H., Powell, M.D., Pietrzak, J.D., 2012. Wind and waves in
461 extreme hurricanes. Journal of Geophysical Research: Oceans 117.
- 462 Janssen, P.A., 1991. Quasi-linear theory of wind-wave generation applied
463 to wave forecasting. Journal of physical oceanography 21, 1631–1642.
- 464 Johns, W.E., Schott, F., 1987. Meandering and transport variations of the
465 Florida Current. Journal of physical oceanography 17, 1128–1147.
- 466 Knaff, J.A., Sampson, C.R., Musgrave, K.D., 2018. Statistical tropical
467 cyclone wind radii prediction using climatology and persistence: Updates
468 for the western North Pacific. Weather and Forecasting 33, 1093–1098.
- 469 Knutson, T.R., McBride, J.L., Chan, J., Emanuel, K., Holland, G., Landsea,
470 C., Held, I., Kossin, J.P., Srivastava, A., Sugi, M., 2010. Tropical cyclones
471 and climate change. Nature geoscience 3, 157–163.

- 472 Komen, G., Hasselmann, S., Hasselmann, K., 1984. On the existence of a
473 fully developed wind-sea spectrum. *Journal of physical oceanography*
474 14, 1271–1285.
- 475 Kourafalou, V.H., Kang, H., 2012. Florida Current meandering and evo-
476 lution of cyclonic eddies along the Florida Keys Reef Tract: Are they
477 interconnected? *Journal of Geophysical Research: Oceans* 117.
- 478 Kundu, P.K., 1976. Ekman veering observed near the ocean bottom. *Journal*
479 *of Physical Oceanography* 6, 238–242.
- 480 Landsea, C.W., Franklin, J.L., 2013. Atlantic hurricane database uncertainty
481 and presentation of a new database format. *Monthly Weather Review*
482 141, 3576–3592.
- 483 Langmuir, I., 1938. Surface motion of water induced by wind. *Science* 87,
484 119–123.
- 485 Lee, T.N., Leaman, K., Williams, E., Berger, T., Atkinson, L., 1995. Florida
486 Current meanders and gyre formation in the southern Straits of Florida.
487 *Journal of Geophysical Research: Oceans* 100, 8607–8620.
- 488 Lee, T.N., Mayer, D.A., 1977. Low-frequency current variability and spin-off
489 eddies along the shelf off southeast Florida. *Collected Reprints* 1, 344.
- 490 Lee, T.N., Smith, N., 2002. Volume transport variability through the Florida
491 Keys tidal channels. *Continental Shelf Research* 22, 1361–1377.
- 492 Lee, T.N., Williams, E., 1988. Wind-forced transport fluctuations of the
493 Florida Current. *Journal of Physical Oceanography* 18, 937–946.
- 494 Li, Z., Johns, B., 1998. A three-dimensional numerical model of surface
495 waves in the surf zone and longshore current generation over a plane
496 beach. *Estuarine, Coastal and Shelf Science* 47, 395–413.

- 497 Lidz, B.H., Shinn, E.A., 1991. Paleoshorelines, reefs, and a rising sea:
498 South florida, usa. *Journal of Coastal Research* , 203–229.
- 499 Lin, N., Chavas, D., 2012. On hurricane parametric wind and applications in
500 storm surge modeling. *Journal of Geophysical Research: Atmospheres*
501 117.
- 502 Liu, Y., Weisberg, R.H., 2012. Seasonal variability on the West Florida
503 shelf. *Progress in Oceanography* 104, 80–98.
- 504 Liu, Y., Weisberg, R.H., Zheng, L., 2020. Impacts of hurricane Irma on the
505 circulation and transport in Florida Bay and the Charlotte Harbor estuary.
506 *Estuaries and Coasts* 43, 1194–1216.
- 507 Liubartseva, S., Coppini, G., Lecci, R., Clementi, E., 2018. Tracking plastics
508 in the Mediterranean: 2D Lagrangian model. *Marine pollution bulletin*
509 129, 151–162.
- 510 Longuet-Higgins, M.S., 1970. Longshore currents generated by obliquely
511 incident sea waves. *Journal of geophysical research* 75, 6778–6789.
- 512 Longuet-Higgins, M.S., Stewart, R., 1964. Radiation stresses in water
513 waves; a physical discussion, with applications, in: *Deep sea research and oceanographic abstracts*, Elsevier. pp. 529–562.
- 515 Madsen, O.S., Poon, Y.K., Gruber, H.C., 1989. Spectral wave attenuation
516 by bottom friction: Theory, in: *Coastal Engineering 1988*, pp. 492–504.
- 517 Malmstadt, J., Scheitlin, K., Elsner, J., 2009. Florida hurricanes and damage
518 costs. *southeastern geographer* 49, 108–131.
- 519 Marsooli, R., Lin, N., Emanuel, K., Feng, K., 2019. Climate change exac-
520 erbates hurricane flood hazards along US Atlantic and Gulf Coasts in
521 spatially varying patterns. *Nature communications* 10, 1–9.

- 522 McWilliams, J.C., Sullivan, P.P., 2000. Vertical mixing by Langmuir circula-
523 tions. *Spill Science & Technology Bulletin* 6, 225–237.
- 524 Mei, C.C., 1989. The applied dynamics of ocean surface waves. volume 1.
525 World scientific.
- 526 Moon, I.J., Ginis, I., Hara, T., Thomas, B., 2007. A physics-based pa-
527 rameterization of air-sea momentum flux at high wind speeds and its
528 impact on hurricane intensity predictions. *Monthly weather review* 135,
529 2869–2878.
- 530 Pinelli, J.P., Roueche, D., Kijewski-Correa, T., Plaz, F., Prevatt, D., Zisis,
531 I., Elawady, A., Haan, F., Pei, S., Gurley, K., et al., 2018. Overview
532 of damage observed in regional construction during the passage of
533 Hurricane Irma over the State of Florida, in: *Forensic Engineering 2018:*
534 *Forging Forensic Frontiers*. American Society of Civil Engineers Reston,
535 VA, pp. 1028–1038.
- 536 Powell, M.D., Houston, S.H., Amat, L.R., Morisseau-Leroy, N., 1998. The
537 HRD real-time hurricane wind analysis system. *Journal of Wind Engi-
538 neering and Industrial Aerodynamics* 77, 53–64.
- 539 Powell, M.D., Vickery, P.J., Reinhold, T.A., 2003. Reduced drag coefficient
540 for high wind speeds in tropical cyclones. *Nature* 422, 279–283.
- 541 Röhrs, J., Christensen, K.H., Hole, L.R., Broström, G., Drivdal, M., Sundby,
542 S., 2012. Observation-based evaluation of surface wave effects on
543 currents and trajectory forecasts. *Ocean Dynamics* 62, 1519–1533.
- 544 Schott, F.A., Lee, T.N., Zantopp, R., 1988. Variability of structure and
545 transport of the Florida Current in the period range of days to seasonal.
546 *Journal of Physical Oceanography* 18, 1209–1230.
- 547 Shinn, E.A., 1988. The geology of the Florida Keys. *Oceanus* 31, 46–53.

- 548 Siadatmousavi, S.M., Jose, F., Stone, G., 2011. Evaluation of two WAM
549 white capping parameterizations using parallel unstructured SWAN with
550 application to the Northern Gulf of Mexico, USA. *Applied Ocean Research*
551 33, 23–30.
- 552 Sikirić, M.D., Roland, A., Janeković, I., Tomazić, I., Kuzmić, M., 2013.
553 Coupling of the Regional Ocean Modeling System (roms) and Wind
554 Wave Model. *Ocean Modelling* 72, 59–73.
- 555 Smith, N.P., 1982. Response of Florida Atlantic shelf waters to hurricane
556 David. *Journal of Geophysical Research: Oceans* 87, 2007–2016.
- 557 Stokes, G.G., 1880. On the theory of oscillatory waves. *Transactions of the*
558 *Cambridge philosophical society* .
- 559 Tolman, H.L., et al., 2009. User manual and system documentation of
560 WAVEWATCH III TM version 3.14. Technical note, MMAB Contribution
561 276, 220.
- 562 Van Den Bremer, T., Breivik, Ø., 2018. Stokes drift. *Philosophical Trans-*
563 *actions of the Royal Society A: Mathematical, Physical and Engineering*
564 *Sciences* 376, 20170104.
- 565 Villas Bôas, A.B., Cornuelle, B.D., Mazloff, M.R., Gille, S.T., Arduin, F.,
566 2020. Wave–current interactions at meso-and submesoscales: Insights
567 from idealized numerical simulations. *Journal of Physical Oceanography*
568 50, 3483–3500.
- 569 Weisberg, R., Liu, Y., Mayer, D., 2009. Mean circulation on the west Florida
570 continental shelf observed with long-term moorings. *Geophys. Res. Lett*
571 36, L19610.
- 572 Weisberg, R.H., Zheng, L., 2006. Hurricane storm surge simulations for
573 Tampa Bay. *Estuaries and Coasts* 29, 899–913.

- 574 Wu, L., Chen, C., Guo, P., Shi, M., Qi, J., Ge, J., 2011. A FVCOM-based
575 unstructured grid wave, current, sediment transport model, I. Model
576 description and validation. *Journal of Ocean University of China* 10, 1–8.
- 577 Xian, S., Feng, K., Lin, N., Marsooli, R., Chavas, D., Chen, J., Hatzikyriakou,
578 A., 2018. Brief communication: Rapid assessment of damaged residential
579 buildings in the Florida Keys after Hurricane Irma. *Natural Hazards and*
580 *Earth System Sciences* 18, 2041–2045.
- 581 Zedler, S., Niiler, P., Stammer, D., Terrill, E., Morzel, J., 2009. Ocean's
582 response to Hurricane Frances and its implications for drag coefficient
583 parameterization at high wind speeds. *Journal of Geophysical Research: Oceans* 114.
- 585 Zhang, C., Durgan, S.D., Lagomasino, D., 2019. Modeling risk of mangroves
586 to tropical cyclones: A case study of Hurricane Irma. *Estuarine, Coastal
587 and Shelf Science* 224, 108–116.